J. Fluid Mech. (2010), *vol.* 647, *pp.* 163–185.
doi:10.1017/S0022112009993594

Events before droplet splashing on a solid surface

MADHAV MANI, SHREYAS MANDRE
AND MICHAEL P. BRENNER†

School of Engineering and Applied Sciences, Harvard University, Cambridge MA 02138, USA

(Received 16 July 2009; revised 18 November 2009; accepted 20 November 2009)

A high-velocity ($\approx 1\,\mathrm{m\,s^{-1}}$) impact between a liquid droplet ($\approx 1\,\mathrm{mm}$) and a solid surface produces a splash. Classical observations traced the origin of this splash to a thin sheet of fluid ejected near the impact point, though the fluid mechanical mechanism leading to the sheet is not known. Mechanisms of sheet formation have heretofore relied on initial contact of the droplet and the surface. In this paper, we theoretically and numerically study the events within the time scale of about 1 μs over which the coupled dynamics between the gas and the droplet becomes important. The droplet initially tries to contact the substrate by either draining gas out of a thin layer or compressing it, with the local behaviour described by a self-similar solution of the governing equations. This similarity solution is not asymptotically consistent: forces that were initially negligible become relevant and dramatically change the behaviour. Depending on the radius and impact velocity of the droplet, we show that the solution is overtaken by initially subdominant physical effects such as the surface tension of the liquid–gas interface or viscous forces in the liquid. At low impact velocities surface tension stops the droplet from impacting the surface, whereas at higher velocities viscous forces become important before surface tension. The ultimate dynamics of the interface once droplet viscosity cannot be neglected is not yet known.

1. Introduction

At sufficiently high impact velocities, a droplet colliding with a solid surface produces a splash. The commonality of splashing of droplets belies the fact that there is another potential solution to the equations of fluid mechanics for the impact of droplets on a solid surface, that the droplet simply spreads smoothly outwards along the surface. Several studies (Gopinath & Koch 2002; Bach, Koch & Gopinath 2004; Pan & Law 2007) have studied the approach of a droplet at low to moderate velocities where surface tension dominates and a plethora of phenomena such as droplet bouncing are observed. Here we are investigating a different parameter regime, and our goal is to have a better understanding of the explosive phenomena of splashing.

Why does splashing occur? Bowden & Field (1964), Jenkins & Booker (1960), Lesser (1981), Field, Dear & Ogren (1989) and Lesser & Field (1983) discovered that when a splash occurs, a thin fluid sheet is emitted very near the point at which the droplet contacts the solid surface, with the sheet subsequently breaking down into a spray of droplets. Figure 1 shows a snapshot of a sheet (Xu, Zhang & Nagel 2005), which has been ejected into the gas before disintegrating into satellite drops; the sheet generation occurs much earlier in the impact process. Although known for nearly half

† Email address for correspondence: brenner@seas.harvard.edu

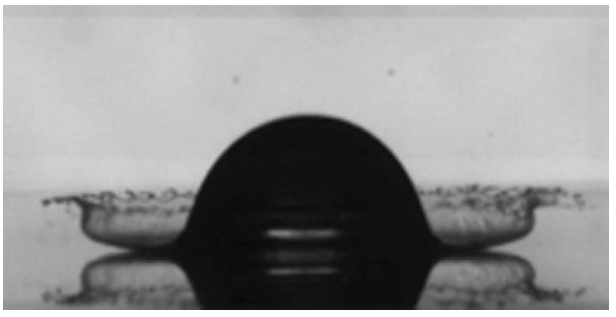

FIGURE 1. Sheet ejection and evolution thereof from a splash, taken from Xu *et al.* (2005), 0.276 ms after initial contact, for an ethanol droplet of 3.4 mm diameter hitting a solid surface at $V_0 = 3.74\,\mathrm{m\,s^{-1}}$.

a century, the fluid mechanical origin of the thin sheet is not yet understood. On the experimental side, the events surrounding the sheet ejection occur so quickly and at such small length scales that they have thus far proven to be impossible to measure. On the theoretical side, to our knowledge, there are not currently even credible estimates for even the basic length scales and time scales at which the phenomena leading to sheet ejection occur.

Why are these sheets formed? It is often argued that thin-sheet ejection is inevitable because of volume conservation: once the droplet impacts, the fluid that would have traversed below the solid surface must be displaced. But fluid could just as easily be pushed upwards into the body of the droplet, instead of forming a thin fluid sheet. Furthermore, it does not give a mechanism for a sheet being propelled into the gas instead of along the solid. Despite the lack of a mechanistic understanding, empirical studies have well studied the conditions for sheet formation and splashing. There is a critical velocity, the 'splash threshold', above which splashing occurs; such thresholds (Levin and Hobbs 1971; Stow & Hadfield 1981; Yarin & Weiss 1995; Bussmann, Chandra & Mostaghimi 2000; Deegan, Brunet & Eggers 2008; Rein & Delplanque 2008) have long been known to depend on surface tension, density, liquid viscosity and surface roughness. Surprisingly, recent experiments by Xu *et al.* (2005) demonstrated a regime in which the splash threshold also depends on the ambient gas pressure; below a threshold gas pressure, splashing is suppressed. More insight about the possible role of the ambient gas is provided by high-speed photography (Thoroddsen *et al.* 2005), which gives a detailed picture of the dynamics of an entrapped air bubble between the liquid and the solid surface but is unable to resolve the earliest stages of the formation of the air bubble or sheet generation itself.

Current rationale for sheet formation heavily relies on the droplet physically contacting the solid surface and the associated contact singularity. The contact singularity arises because of the following simple argument. After a time t, a droplet of radius R falling at velocity V has penetrated the solid surface a distance Vt. The radius of the wetted area is $r_{wet} = \sqrt{2RVt}$, giving $\mathrm{d}r_{wet}/\mathrm{d}t = \sqrt{RV/2t}$. As $t \to 0$, the velocity at the edge of the wetted area diverges. This is a real singularity due to the geometry of a parabolic surface impacting a plane. One popular mechanism for sheet formation points out that the contact line velocity is much larger than the liquid sound velocity; this means that the pressure disturbance from the collision of the droplet with the solid surface is initially pinned to the contact line, so that there can

be no (localized) distortion of the liquid surface. Once $\mathrm{d}r_{wet}/\mathrm{d}t$ slows below the liquid sound velocity, there is an abrupt increase in the pressure at the liquid–gas interface; such an impulse could cause the generation of a liquid sheet (Lesser 1981; Rein 1993; Haller *et al.* 2003).

The difficulty with this model is that observations show a liquid sheet launched into the gas (figure 1), whereas the above-mentioned arguments suggest that the sheet will be propelled along the solid surface. Such a liquid film will experience enormous frictional forces which strongly resist deformation of the sheet off the solid surface. Viscous stresses in the surrounding gas are necessarily smaller than those within the liquid; so it is hard to understand how the viscous response of the gas could counteract the friction with the solid surface. This issue, coupled with the role of ambient gas pressure (Xu *et al.* 2005), led us to the hypothesis that the liquid sheet might originate because of the interaction of the liquid with the intervening gas layer, 'before' the droplet contacts the solid surface (Mandre, Mani & Brenner 2009).

The goal of the current investigation is therefore to study the approach of a droplet to a solid surface through an intervening gas layer, to search for potential fluid mechanical mechanisms for sheet generation before contact. We describe the dynamic state of the drop interface by the curve $y = h(x, t)$, where y is the coordinate normal to the wall, x being along the wall and t being time. By asymptotically deriving a reduced mathematical model for $h(x, t)$ from the Navier–Stokes equations and solving it, we follow the dynamical history of the drop and decide whether the dynamics we observe is indicative of sheet generation. The ultimate goal is to model the following possible outcomes of our model.

(i) The drop contacting the surface in finite time: this corresponds to $h(x, t) \to 0$ for some $x = x_0$ at a finite $t = t_0$.

(ii) The interface overturning on itself: mathematically, this implies $h_x(x, t) \to \infty$ for some $x = x_0$ at finite $t = t_0$, while $h(x_0, t_0)$ remains positive. If the interface overturns, we are unable to evolve the dynamics any further owing to the limitations of a single-valued description of the interface. Moreover, the interface becoming multi-valued is not necessarily an indication of splashing. In experiments, the interface is observed to overturn on itself both during the splashing and spreading phases.

While neither of these two outcomes is an indication of splashing, sheet generation is a necessary but not sufficient condition for splashing. In the current paper, we make a first attempt to describe these dynamics in the presence of the dominant forces, viz. inertia of the droplet, the surface tension on the interface and the viscosity and the compressibility of the gas. We demonstrate that a remarkably rich cascade of events occur well before contact with the solid surface occurs.

Figure 2 shows simulations, described in detail later in the paper, of an ethanol droplet of a radius 1.7 mm hitting a solid surface with a speed of $3.74\,\mathrm{m\,s^{-1}}$. On time scales of $\sim$0.1 μs and length scales of $\sim$100 μm, deformations of the liquid interface occur when the surface is about 1 μm away from the drop. We observe that the behaviour of the interface depends critically on both impact parameters (droplet radius and velocity) and fluid and gas properties. Depending on the parameters, important effects include liquid inertia, liquid viscosity, interfacial surface tension, gas pressure, gas viscosity, compressibility of the gas, heat transfer in the gas, mass transfer between the gas and the liquid and the mean free path of the gas. The present work extends the results of our recent paper (Mandre *et al.* 2009), which demonstrated that liquid surface tension prohibits contact with the solid surface, causing the droplet to skate on a very thin gas layer. We show that depending on the droplet radius and impact velocity, other physical effects – in particular, viscous

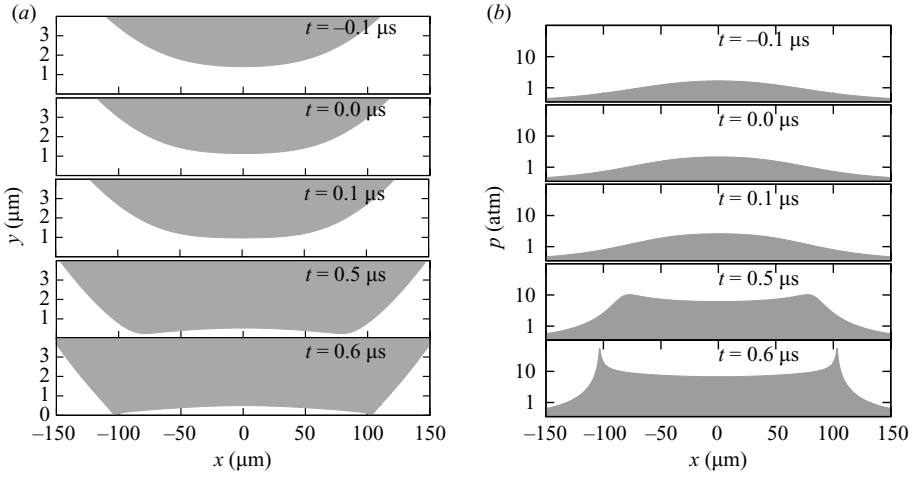

FIGURE 2. Snapshots from simulations documenting the deformation of a droplet ($R = 1.7 \times 10^{-3}$ m, $\mu_g = 1.8 \times 10^{-5}$ Pa s, $V = 3.74\,\mathrm{m\,s^{-1}}$, $\rho_\ell = 780\,\mathrm{kg\,m^{-3}}$) before contacting the solid surface. Time is measured relative to the moment of contact if no gaseous layer is present. Over time scales of $\sim 0.1\,\mu$s, (*a*) shows deformations in the interface of the droplet occurring on the scales of micrometres. Depending on impact, fluid and gas parameters, we demonstrate that further phenomena set in when the gas gap is of order 10–100 nm. The build-up of the gas pressure as the minimum gap thickness decreases is shown in (*b*).

forces in the liquid – can also stop the similarity solution, leading potentially to other qualitative behaviours, such as, hypothetically, sheets.

The organization of the paper is as follows. In the next section, we summarize our mathematical model. We consider the full Navier–Stokes equations for the flows in the liquid and the intervening gas layer; we then use the initial condition, in which the droplet is moving towards the solid at high velocity, to argue that the dominant forces initially are the inertia of the liquid, as well as compressible and viscous forces in the gas. Section 3 discusses the very initial stages of the droplet's interaction with the solid surface, when the liquid interface first deforms because of the pressure in the gas layer. We demonstrate that depending on both the impact parameters of the droplet and the properties of the liquid and the gas, the dynamics in the gas layer can be either compressible or incompressible; experiments (Xu *et al.* 2005) tend to occur in the regime in which the gas is initially compressible. Section 4 considers the subsequent evolution of the liquid interface after it initially deforms. The liquid layer attempts to contact the solid substrate by either forcing the gas to drain out of the layer or compressing it, with the local behaviour described by a self-similar solution of the governing equations. The structure of this similarity solution is derived and compared with high-resolution numerical simulations. Section 5 demonstrates that the similarity solution is not asymptotically consistent: the solution causes forces that were initially deemed negligible to become important; this includes the surface tension of the liquid–gas interface and viscous forces in the liquid. We report phase diagrams predicting the thickness of the gas film when each of these forces becomes important, and we indicate the dominant effect as a function of experimental parameters. Surface tension dominates at low impact speeds ($\sim 1\,\mathrm{m\,s^{-1}}$), which we have previously demonstrated

stops liquid–solid contact Mandre *et al.* (2009), causing the droplet to skate along a thin film of gas; at higher impact speeds we show that viscous forces in the liquid become important before surface tension.

2. Mathematical model

We consider the fluid mechanics of an initially spherical droplet of radius R approaching a wall with speed V in a gaseous environment at pressure P_0. As the droplet approaches the wall, fluid forces build up in the gas film between the drop and the wall and cause the droplet to deform. The principal goal of our analysis is to discover whether these forces are capable of creating a thin fluid sheet. As emphasized in the Introduction, the number of potentially relevant physical effects is quite large, and it is not clear *a priori* which are the most relevant.

To discover the relevant effects we proceed in the following fashion. We first consider the full equations of motion for both the droplet and the gas layer. Given the initial state of the droplet, some of the terms in the equation of motion are demonstrably unimportant. The major simplifications for a typical millimetre-sized droplet with impact velocity of order $1\,\mathrm{m\,s^{-1}}$ are (i) slender geometry for the gas film, (ii) the neglect of viscous forces in the liquid, (iii) the neglect of surface tension forces at the liquid–gas interface and (iv) the neglect of nonlinear inertia in the liquid. With respect to viscous forces, the liquid Reynolds number is of order $Re = \rho_\ell RV/\mu_\ell = 1000$, where μ_ℓ, ρ_ℓ are the liquid viscosity and density respectively; hence inertial forces in the fluid initially overwhelm viscous forces, and we therefore neglect viscosity. With respect to the relative sizes of inertial pressures to pressure variations caused by surface tension, the relevant dimensionless number is the Weber number $We = \rho_\ell V^2/\sigma$, where σ is the liquid surface tension. For a typical droplet in the splashing regime $We \sim 100$, and hence surface tension is negligible. Finally, the nonlinear effect of inertia is initially small because before its interaction with the wall, the velocity field inside the droplet is 'constant'.

Using these approximations, we solve the equations of motion for the evolution of the droplet as it impacts the wall. We then monitor the resulting solutions for the continued validity of the approximations: for each of the major approximations made, we will see that the approximation breaks down at some time before the droplet contacts the wall. The precise distance between the droplet and the wall at which this occurs depends on the parameter regime, as does the neglected force that first becomes important. For example at low impact velocities we will see that the neglect of surface tension is the first force to become important, whereas at higher impact velocities viscous stresses in the liquid are the first. Once our computed solution is invalidated by the breakdown of an approximation, the continued evolution of the droplet impact requires a different approach.

It is worth remarking that in addition to the approximations listed above, there are a number of additional physical effects that we neglect in the present analysis that might ultimately prove to be important for splashing. These effects include (i) heat transfer in the gas, which affects the gas equation of state, and (ii) mass diffusion from the gas into the liquid (we assume in our calculations that the gas layer cannot be absorbed into the liquid). The neglect of all of these effects is valid in the regime we are calculating, though these approximations could well breakdown before contact and hence be important for any putative sheet formation mechanism.

2.1. *Dynamics in the liquid*

The aforementioned approximations imply that in the liquid, we need to study the incompressible Euler equations. At this point, we make one further approximation, this time for computational convenience: we model the spherical droplet as a cylinder. Approximating the dynamics as two-dimensional allows us to employ complex analytic methods (e.g. see Smith, Li & Wu 2003) in solving for the inviscid dynamics in the liquid. The central quantitative results of the current paper are not affected by the two-dimensional approximation: the similarity solution at the heart of the present paper (dictating when the various neglected fluid forces become important) applies quantitatively to both cylindrical and spherical impact. The subscripts ℓ and g refer to the variables in the drop and the gas respectively, and the subscripts x, y, ξ and t denote differentiation with respect to the respective coordinate. The two-dimensional Euler equations for the liquid velocity components $\boldsymbol{u} = (u_\ell, v_\ell)$ and liquid pressure p_ℓ are

$$\rho_\ell \boldsymbol{u}_t + \nabla p_\ell = -\rho_\ell \boldsymbol{u}\cdot\nabla\boldsymbol{u} + \mu_\ell \nabla^2 \boldsymbol{u}, \quad \nabla\cdot\boldsymbol{u} = 0, \tag{2.1}$$

where the terms on the right-hand side of the first equation (fluid viscosity and the nonlinear effect of inertia) will be deemed negligible, as described above. Keeping account of the terms assumed negligible allows us to later evaluate the validity of our assumptions. These equations can be rewritten in a computationally tractable form using complex analytic methods: since $\nabla^2 p_\ell \approx 0$, we can define its harmonic conjugate q_ℓ such that the function $p_\ell + \mathrm{i}q_\ell$ is holomorphic in the complex plane $z = x + \mathrm{i}y$. Dropping the subscript for now, Cauchy's integral formula gives

$$\frac{\mathrm{d}}{\mathrm{d}z}(p_\ell + \mathrm{i}q_\ell) = \frac{1}{2\pi\mathrm{i}} \int_{-\infty}^{+\infty} \frac{p_{\ell\xi}(\xi, 0, t) + \mathrm{i}q_{\ell\xi}(\xi, 0, t)}{(\xi - z)} \mathrm{d}\xi. \tag{2.2}$$

Grouping the imaginary terms and evaluating them at the interface, $y = 0$, gives us an expression for the vertical pressure gradient at the liquid interface, in terms of the horizontal pressure gradient evaluated at the interface. Namely, we have

$$p_{\ell y}(x, 0, t) = \frac{1}{\pi} \fint_{-\infty}^{+\infty} \frac{p_\xi}{(\xi - x)} \mathrm{d}\xi, \tag{2.3}$$

where the principal value of the integral is considered on the right-hand side. Recognizing the right-hand side of (2.3) as the Hilbert transform of $p_{\ell x}$ and using (2.1) we arrive at an equation prescribing the acceleration of the interface subject to a horizontal pressure gradient at the interface,

$$\rho_\ell h_{tt} - \mathscr{H}[p_{\ell x}] = -\rho_\ell (u_\ell v_{\ell x} + v_\ell v_{\ell y}) + \mu_\ell \nabla^2 v_\ell - \rho_\ell (u_\ell h_x)_t, \tag{2.4}$$

where we have made use of the kinematic boundary condition $\partial h/\partial t = v_\ell - u h_x$ and written in a form such that the terms on the right-hand side will be deemed negligible.

2.2. *Dynamics in the gas and at the interface*

Now let us consider the dynamics in the gas. When the droplet is close to the wall, the vertical length scale (set by the distance from the droplet to the wall) is much smaller than the horizontal length scale (set by the radius of curvature of the droplet). Mass conservation then suggests that the horizontal flow velocities in the gas are much larger than the vertical velocities. The gas follows its equations of state and can exhibit compressible behaviour if the characteristic pressure scale exceeds the ambient

gas pressure. The compressible lubrication equations are (Taylor & Saffman 1957)

$$\rho_{g,t} + (\rho_g u_g)_x + (\rho_g v_g)_y = 0, \tag{2.5}$$

$$-p_{g,x} + \mu_g u_{g,yy} = \rho_g(u_{g,t} + u_g u_{g,x} + v_g u_{g,y}) - \mu_g u_{g,xx}, \tag{2.6}$$

where the right-hand side of (2.6) is negligible for the dynamics under consideration. Since $\mu_l \gg \mu_g$, and furthermore the scale for horizontal velocity is much larger in the gas than in the drop, we employ a no-slip boundary condition on the interface,

$$u_g = 0, \quad v_g = h_t \text{ at } y = h(x,t) \quad \text{and} \quad u_g = v_g = 0 \text{ at } y = 0. \tag{2.7}$$

The leading-order solution to (2.6) is

$$u_g = -\frac{p_{g,x}}{2\mu_g} y(h - y) + \text{corrections}, \tag{2.8}$$

where the corrections are estimated by substituting the leading-order solution back into the right-hand side of (2.6). Integrating (2.5) across the gap subject to (2.7) finally gives us the evolution equation for the gas,

$$(\rho_g h)_t - \frac{1}{12\mu_g}\left(\rho_g h^3 p_{g,x}\right)_x = -\left[\rho_g\left(\frac{h^5 p_{g,xxx}}{120\mu_g} + \frac{h^4 p_{g,x} h_{xx}}{48\mu_g}\right)\right]_x - \left[\rho_g^2\left(\frac{h^5 p_{g,xt}}{120\mu_g^2} + \frac{h^4 p_{g,x} h_t}{48\mu_g^2}\right)\right]_x, \tag{2.9}$$

where again the terms on the right-hand side are the first-order corrections to the compressible lubrication theory we employ. We do not use these terms except to later verify the validity of our approximation. The first term on the right-hand side comes from the viscous term in (2.6), and the second comes from the acceleration of the gas. Equations (2.4) and (2.9) are solved subject to the Laplace condition for pressure $p_\ell = p_g + \sigma h_{xx}$ and the equation of state for the gas $p_g = P_0(\rho_g/\rho_0)^\gamma$, where γ is a constant and models the heat transfer. We choose $\gamma = 1$ for an isothermal gas film and $\gamma = 1.4$ for an adiabatic gas film.

We solve this model starting with the initial conditions

$$h(x,t) = h_0 + \frac{x^2}{2R}, \quad h_t(x,t) = -V, \quad p(x,t) = P_0, \quad \rho(x,t) = \rho_0, \tag{2.10}$$

where h_0 is chosen sufficiently large so that the drop can be assumed to initially move with constant speed. We have approximated the interface shape to be a parabola, since we anticipate $h_0 \ll R$ as is traditionally assumed in the lubrication theory. We justify our assumptions in the next section.

3. Initial deformation

To gain intuition for the flows that are set up between the liquid droplet and the gas layer, we first focus on the very initial stages of impact, when the droplet first deforms from its spherical initial shape, because of its interaction with the underlying gas layer. Figure 2 shows subsequent snapshots in time of the interfacial and pressure profiles. The first snapshot is when the droplet first begins to deform away from its uniform curvature state; a unimodal profile for the pressure develops that signals the onset of lubrication forces in the gas. Later snapshots show clearly the development of a dimple at the origin at a height $H = H^*$ from the solid surface, which stays roughly constant.

What sets the thickness H^* at which droplet deformation begins? This thickness is also what sets the height of the layer of gas trapped under the droplet. For the droplet to deform, the pressure in the gas must be sufficient to decelerate the falling liquid, locally, from velocity V to rest; that is to say the gas pressure must balance the inertial pressure in the droplet. Owing to its parabolic shape, the approaching droplet, in interaction with the gas layer below, sets up a flow over a horizontal length scale $L = \sqrt{RH}$ in the gas. We now carry out a simple scaling analysis of the equations of motions described above. The left-hand side of the drop equation (2.4) gives the inertial pressure gradient in the drop,

$$P_\ell / L \sim \rho_\ell h_{tt} \sim \rho_l V/\tau, \tag{3.1}$$

where $h_t \sim V$ is the velocity scale in the system and $\tau = H/V$ is the time scale over which the fluid is brought to rest. When the drop is sufficiently far from the solid surface the gas density is undisturbed, $\rho_g \approx \rho_0$, so that the gas pressure is set by incompressible viscous drainage. Equation (2.9) then implies that

$$P_g / L \sim \mu RV / LH^2. \tag{3.2}$$

The liquid interface distorts when the gas pressure is of order the inertial pressure, $P_g \sim P_\ell$. This balance gives an estimate for the height at which the dimple forms and the pressure in the dimple,

$$H^*_{Incomp} = RSt^{2/3}, \quad P^*_{Incomp} = \frac{\mu V}{RSt^{4/3}}, \tag{3.3}$$

where $St = \mu_g/(\rho_\ell V R)$ is the inverse of the Stokes number. Physically, St is the ratio of the viscous forces in the gas to the inertial forces in the drop.

The observation that altering the ambient pressure alters the dynamics leads us to question whether compressible effects are important in the deformation of the droplet and its subsequent behaviour. Using the threshold values for splashing reported by Xu *et al.* (2005) ($P_0 = 30$ kPa) and the incompressible scalings derived above we can compute the dimple pressure, P^*_{Incomp}, as being the value of the pressure at the dimple's location when the droplet first deviates from its circular state. We find $P^*_{Incomp} = 700$ kPa. The pressure required to produce a dimple is significantly greater than the typical threshold ambient pressure, thereby making it apparent that the neglected compressible effects must be important. If the pressure in the gas, P_{gas}, is of the order of the ambient pressure, then before the drop can deform, the underlying gas compresses. This transition happens when $P_{gas} \sim P_0$ or when

$$H_* = R(\mu V / RP_0)^{1/2}. \tag{3.4}$$

This critical height (indicated by the subscript star) marks the transition from incompressible dynamics to a compressible one. Below this critical height viscous drainage can be neglected, and the gas equation (2.9) simplifies to

$$(\rho_g h)_t \approx 0 \tag{3.5}$$

or $\rho_g h = \rho_0 H_*$, where ρ_0 is the initial gas density. Balancing the gas pressure gradient with the liquid deceleration as before we arrive at

$$H^*_{comp} = RSt^{2/3} \epsilon^{(2-\gamma)/(2\gamma-1)} \text{ where } \epsilon \equiv \frac{P_0}{(R\mu^{-1}V^7\rho_0^4)^{1/3}}. \tag{3.6}$$

This dimensionless parameter ϵ may be interpreted as the ratio of the ambient pressure (P_0) to the pressure that would have built up in the film if the gas film

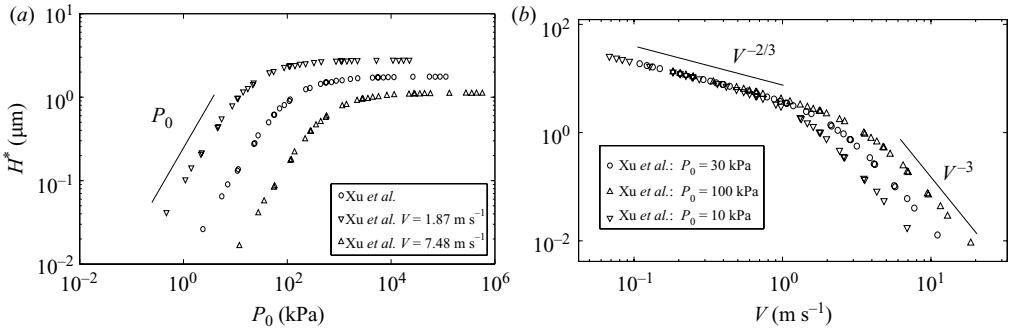

FIGURE 3. (*a*) Dimensional dimple height H^* (in micrometres) as a function of the ambient pressure P_0 (in kilopascals). The open circles correspond to $V_{impact} = 3.74\,\mathrm{m\,s^{-1}}$; other data sets correspond to altered values of impact velocity. The dimple height decreases as impact velocity is increased and *vice versa*. (*b*) Dimensional dimple height H^* (in micrometres) as a function of the impact velocity V (in metres per second). The open circles correspond to $P_0 = 30$ kPa; other data sets correspond to altered values of ambient air pressure. The dimple height increases with increasing ambient air pressure, this is apparent for $V > 1$; however for low velocities any dependence on air pressure appears to be negligible. Other parameter values are characteristic of experiments conducted by Xu *et al.* (2005) ($R_{drop} = 1.7 \times 10^{-3}$ m, $\mu_{gas} = 1.8 \times 10^{-5}$ Pa s, $\rho_{drop} = 780\,\mathrm{kg\,m^{-3}}$).

were incompressible (P^*_{Incomp} from (3.3)); it determines the importance of compressible effects in the system compared with lubrication drainage. The height at which the dimple forms depends on the value of the ambient pressure.

In order to verify the scaling predictions presented above we simulated the above-given equation for a range of St and ϵ, tracking the height $H = H^*$ at which the droplet's interface first deviates from a circular shape. To illustrate the numerical values of the dimple height in typical experiments, we carried out a series of simulations, varying the ambient pressure and the impact speed and tracking the height at which the dimple first forms. Figure 3(*a*) shows H^* in micrometres as a function of the ambient pressure P_0 in kilopascals, for ethanol droplets identical to those used in Xu *et al.* (2005). For sufficiently large P_0, the dimple height is independent of P_0 in accordance with the incompressible scaling, whereas for sufficiently small P_0 the dimple height decreases scaling as $P_0^{(2-\gamma)/(2\gamma-1)}$ according to (3.6). The value of pressure that demarcates this behaviour depends on the impact speed. Similarly figure 3(*b*) shows that the dimple height decreases with velocity as $V^{-2/3}$ but is independent of the ambient pressure for impact speeds slower than a critical value. Above this critical value, the power law changes to $V^{-(16-7\gamma)/(3(2\gamma-1))}$. The critical value of velocity depends on the ambient pressure.

All these data can be collapsed on to a single master curve by plotting $H^*/RSt^{2/3}$ as a function of ϵ as shown in figure 4 (reproduced from Mandre *et al.* 2009). We show results for $\gamma = 1$ and $\gamma = 1.4$ in this figure to demonstrate that the small and large ϵ asymptotes are in agreement with (3.3) and (3.6). Thus we conclude that ϵ captures the transition from an incompressible regime to a compressible one. The dynamics is incompressible for $\epsilon \gg 1$ and compressible for $\epsilon \ll 1$.

Thoroddsen, Etoh & Takehara (2003) investigated the impact of a droplet on a liquid surface which can entrap a small amount of air under its centre as the two liquid surfaces meet, followed by a similar measurement for impact with a dry solid surface (Thoroddsen *et al*. 2005) . They measured the thickness of the trapped air film

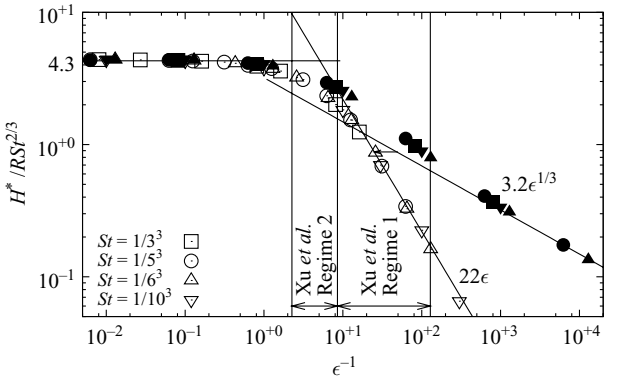

FIGURE 4. Dimensionless dimple height $\bar{H} = H^*/RSt^{2/3}$ versus ϵ for a range of St. The open symbols denote $\gamma = 1$, while the corresponding filled symbols denote $\gamma = 1.4$. The data collapse on to a single curve for a given value of γ, with the asymptotes agreeing with the predictions. The data confirm that the dynamics is independent of the ambient pressure when the system is incompressible, seen by the data asymptoting to a constant for large values of ϵ.

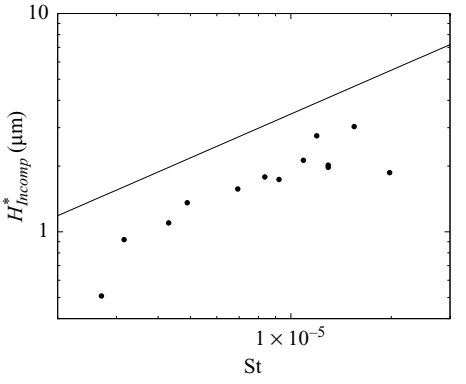

FIGURE 5. Comparison with experiments by Thoroddsen *et al.* (2003) of the height of an entrapped bubble when a droplet impacts a deep pool of the same liquid. The dots are experimental results for the average initial thickness of the air sheet entrapped versus St for a droplet of diameter $D = 3.47$ mm. The solid line is our theoretical prediction for the height of this air sheet ($H^*_{Incomp} = RSt^{2/3}$), since the dynamics is identical to droplet impact with a liquid pool within our approximations.

for different drop velocities. Although our calculations account for a two-dimensional planar geometry, while real drops are closer to axisymmetric, the scalings of these quantities are identical, and only the prefactors of the scaling laws are different. The values they measured for the impact with a solid wall compare very well with our calculations; however there is too much variation in their measurement to compare the scaling behaviour. Since, within our approximation, the dynamics for impact with a solid surface is identical with the dynamics for impact with a deep liquid pool, and the latter measurements have much less scatter, we have compared the results of our calculations with their results. Figure 5 presents their measurements of the air film thickness and our prediction $H^*_{Incomp} = RSt^{2/3}$, and they agree upto a scaling prefactor. The agreement in figure 5 provides evidence towards the theory presented here for liquid–solid impact being pertinent to other situations such as liquid–liquid impact.

With the scalings derived and confirmed we rescale the governing equations for the droplet (2.4) and gas (2.9) into dimensionless form. The variables with bars refer to dimensionless variables and those without the bars to their dimensional counterparts. Using

$$h = RSt^{2/3}\bar{h}, \quad x = RSt^{1/3}\bar{x}, \quad p_\ell = \frac{\mu_g V}{RSt^{4/3}}\bar{p}_\ell, \quad t = \frac{RSt^{2/3}}{V}\bar{t}, \quad p_g = P_0\bar{p}, \quad \rho_g = \rho_0\bar{\rho} \tag{3.7}$$

results in

$$h_{tt} - \epsilon\mathscr{H}(p_x) = Re^{-1}\nabla^2 v - St^{1/3}(uv_x + vv_y) + \epsilon\delta\mathscr{H}(h_{xxx}), \tag{3.8}$$

$$(\rho h)_t - \frac{\epsilon}{12}(\rho h^3 p_x)_x = -\epsilon St^{2/3}\left[\rho\left(\frac{h^5 p_{xxx}}{120} + \frac{h^4 h_{xx} p_x}{48}\right)\right]_x - \epsilon Re_g St^{2/3}\left[\rho^2\left(\frac{h^5 p_{xt}}{120} + \frac{h^4 h_t p_x}{48}\right)\right]_x, \tag{3.9}$$

$$p = \rho^\gamma, \tag{3.10}$$

where $Re = \rho_\ell V R/\mu_l$ is the drop Reynolds number; $Re_g = \rho_0 RV/\mu_g$ is the gas Reynolds number; $\delta = \sigma/RP_0$ is the ratio of the Laplace pressure to gas pressure; and we have dropped the bars. For typical drop impacts $St \approx 10^{-5}$, $Re \approx 10^3$ and $\delta \approx 10^{-4}$; hence the terms on the right-hand side are negligible, as we expected. Moreover, only one dimensionless parameters ϵ defined in (3.6) characterizes the behaviour of the solution. Hence, we begin by considering the evolution of the interface and any dependence that it might have on the ambient gas pressure, by considering the limit, $\delta \to 0$, $St \to 0$, $Re_g St^{2/3} \to 0$ and $Re^{-1} \to 0$ and studying the ϵ dependence. Thus we initially focus our attention on the solution of (3.10), coupled with

$$h_{tt} = \epsilon\mathscr{H}(p_x), \tag{3.11}$$

$$(\rho h)_t - \frac{\epsilon}{12}(\rho h^3 p_x)_x = 0. \tag{3.12}$$

4. Beyond the dimple: the similarity solution

We now consider the evolution of the droplet interface after the formation of a dimple. Figure 2 ($\epsilon = 5 \times 10^{-3}$) shows that subsequent to dimple formation, the droplet interface and pressure profiles develop two symmetric kinks that move away from origin at a constant speed; the location of the interface's minima coincides with the maximum of the pressure profile. In an axisymmetric geometry, this suggests a circular rim moving away from the origin. Accompanying this movement outwards, the minimum film thickness h_{min} continues to decrease, and the pressure maximum p_{max} increases. The kink is characterized by a new horizontal length scale ℓ which rapidly decreases as $h_{min} \to 0$, indicated by increasingly higher curvatures developing in figure 2. If we neglect forces other than those considered in (3.10), we find that for every ϵ, the solution forms a singularity in which the interfacial curvature and internal pressure diverges in finite time.

Figure 6 shows the evolutions of p_{max} and ℓ as a function of h_{min}, for a range of different values of $10^{-3} \leqslant \epsilon \leqslant 10^2$. Both the maximum pressure and ℓ eventually behave as power laws, $p_{max} \sim h_{min}^{-\beta}$, $\ell \sim h_{min}^{\alpha}$, where the scaling exponents α, β show a strong dependence on ϵ. At large ϵ, the solution obeys $\beta \approx 0.5$ and $\alpha \approx 1.5$. At the low ϵ characteristic of experiments the behaviour is much more complicated: for example

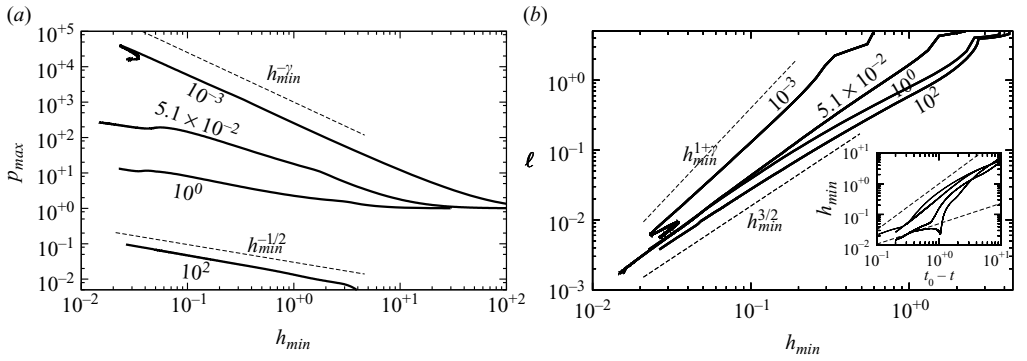

FIGURE 6. (*a*) Maximum pressure p_{max} and (*b*) curvature length scale ℓ as a function of h_{min} shown by the solid lines. The labels denote values of ϵ. The ambient pressure is subtracted from p_{max} for $\epsilon = 100$. The dashed lines denote various power-law estimates (see the text). The value $\epsilon = 5.1 \times 10^{-2}$ corresponds to figure 1 of Xu *et al.* (2005). The inset in (*b*) shows h_{min} against $t_0 - t$, where t_0 is the time to contact.

at $\epsilon = 0.001$ the maximum pressure, p_{max}, does not even increase monotonically with decreasing h_{min}. The solution transitions between regimes with distinct dependencies on ϵ in a dynamical manner, eventually adopting power laws identical to those seen in the incompressible regime. Similarly at the ϵ of the experiment of Xu *et al.* (2005) ($\epsilon = 0.051$) the behaviour is complicated with several apparent regimes. Below, we present an asymptotic description of the solution that sorts out these different regimes.

We proceed by constructing a similarity solution for the behaviour in the vicinity of the leftmost kink. In both regimes, the height and density fields are described by the self-similar ansatz

$$h(x,t) = h_{min}(t)H(\eta), \quad \rho(x,t) = \rho_{max}(t)R(\eta), \quad p(x,t) = p_{max}(t)\Pi(\eta), \tag{4.1}$$

where $\eta = (x - x_0(t))/\ell(t)$ is the similarity coordinate, with $x_0(t)$ being the time-dependent location of the kink. Here ρ_{max} is the time-dependent maximum density. Before we plug this ansatz into the governing equations we can foresee that time derivatives of variables such as $h(x,t)$ will have three contributions,

$$\frac{\partial}{\partial t}h(x,t) = \dot{h}_{min}H - \frac{\eta\dot{\ell}(t)h_{min}}{\ell(t)}H_\eta - \frac{\dot{x}_0 h_{min}}{\ell}H_\eta, \tag{4.2}$$

corresponding to the decrease in the minimum height, a change in time of the characteristic length scale $\ell(t)$ and an advective component corresponding to the movement in the location of the kink away from the origin, respectively. We numerically evaluate the relative size of these terms in every regime we investigate and find that the advective term dominates in every case; that is to say it is at least as large as the other terms, if not larger, as $h_{min} \to 0$. When this term dominates, we hypothesize that the kink region is wave-like in character, that is $\partial_t \approx U\partial_x$, where we recognize that the appropriate scale for x is $\ell(t)$ and that $\dot{x}_0(t) = U$, a constant for a given choice of parameters. The self-similar ansatz along with the knowledge of the wave-like character of the solution can be plugged into the governing equations

(3.10), leading to the following:

$$\frac{(\dot{x}_0)^2 h_{min}}{\ell^2} H_{\eta\eta} = \epsilon \frac{h_{min}\rho_{max}^{\gamma}}{\ell} \mathscr{H}(R_\eta^\gamma), \tag{4.3}$$

$$\frac{U}{\ell}\rho_{max} h_{min}(RH)_\eta = \frac{\epsilon}{12}\frac{\rho_{max}^{1+\gamma} h_{min}^3}{\ell^2}(RH^3 R_\eta^\gamma)_\eta. \tag{4.4}$$

Motivated by the scalings derived above for the formation of the dimple, we expect there to be two broad regimes. If the pressure is dominated by compression of the gas, then we expect that $\rho_{max} h_{min} \sim 1$, so that $p_{max} \sim 1/h_{min}^{\gamma}$. In the other regime, the pressure is dominated by viscous forces. These two regimes occur in taking different limits of the parameter of ϵ, with $\epsilon \gg 1$ corresponding to the incompressible/viscous-dominated regime and $\epsilon \ll 1$ corresponding to the compressible regime.

4.1. *Compressible regime*

We begin by considering the compressible regime where $\epsilon \ll 1$. Motivated by the intuition that the density should increase because of the decreasing h_{min} (i.e. $\rho_{max} h_{min} \sim 1$), we use the ansatz

$$\rho h = \tilde{A}(\epsilon) + f(\epsilon, t)F(\eta). \tag{4.5}$$

Here the first term represents the intuition, whereas the second term is a time-dependent correction whose form we will determine. We require this second term to explain the non-monotonicity in the log–log plots of p_{max} versus h_{min}. The ϵ dependence of the constant $\tilde{A}$ is determined by the state of the gas when the similarity solution sets in: as discussed above, the compressible behaviour sets in at the critical height $H_* = R(\mu V/RP_0)^{1/2}$; this implies that $\tilde{A}(\epsilon) = A\epsilon^{-1/2}$.

To proceed further, we first focus on the developing kink to the left of the origin in figure 2. To the right of this kink, the density is high and the gas is compressible: to its left of the kink the density relaxes to the ambient, and the pressure is determined by viscous stresses. As mentioned previously the density maximum between these two regimes moves outwards as it sharpens, and its advection dominates the time derivatives in the system, that is to say $\partial_t \approx U\partial_x$, where $U = \dot{x}_0$.

The advection approximation and ansatz (4.5) in (3.10) give

$$-\frac{Uf}{\ell}F_\eta = A\frac{\epsilon^{1/2}}{12}\frac{P_{max}h_{min}^2}{\ell^2}\left[H^2\left(\frac{1}{H^\gamma}\right)_\eta\right]_\eta, \tag{4.6}$$

which can be decomposed into a time-dependent scaling and the similarity profile as

$$U\frac{f}{\ell} \sim \epsilon^{1/2}h_{min}^2\frac{P_{max}}{\ell^2}, \quad F_\eta = \frac{A}{12}\left[H^2\left(\frac{1}{H^\gamma}\right)_\eta\right]_\eta. \tag{4.7}$$

Similarly the drop equation in (3.10) yields

$$\frac{P_{max}}{\ell} \sim \epsilon^{-1}U^2\frac{h_{min}}{\ell^2}, \quad H_{\eta\eta} = \mathscr{H}\left[\left(\frac{1}{H^\gamma}\right)_\eta\right]. \tag{4.8}$$

Solving the scalings from (4.5), (4.7) and (4.8) simultaneously for p_{max}, f and ℓ in terms of h_{min} leads to

$$P_{max} \sim \epsilon^{-\gamma/2}h_{min}^{-\gamma}, \quad \ell \sim \epsilon^{(\gamma/2)-1}U^2h_{min}^{1+\gamma}, \quad f \sim \epsilon^{(3/2)-\gamma}U^{-3}h_{min}^{1-2\gamma}. \tag{4.9}$$

Surprisingly, this solution demonstrates that f 'grows' in time; this implies that eventually the intuited $\rho_{max} h_{min} \sim A\epsilon^{-1/2}$ regime will give rise to another regime. The characteristics of this regime can be found by repeating the analysis but neglecting the $A\epsilon^{-1/2}$ term in (4.5), so that $\rho h = f(\epsilon, t)F(\eta)$. All three terms in the time derivative expression given in (4.2) are numerically observed to be equally dominant in this case owing to $\ell \propto t_0 - t$, where t_0 is the time to contact. We then find that

$$U \frac{\rho_{max} h_{min}}{\ell} \sim \epsilon h_{min}^3 \rho_{max} \frac{P_{max}}{\ell^2}, \qquad P_{max} \sim \epsilon^{-1} U^2 \frac{h_{min}}{\ell}. \tag{4.10}$$

These balances give

$$P_{max} \sim \epsilon^{-1} U^{3/2} h_{min}^{-1/2}\ , \ \ell \sim U^{1/2} h_{min}^{3/2}. \tag{4.11}$$

The similarity analysis thus predicts that there are two distinct regimes of compressible behaviour: initially, the solution will follow the first regime, in which $\rho_{max} h_{min} \sim 1$ and the scaling laws (4.9) are obeyed; we call this regime the 'sub-compressible regime'. Below a critical minimum film thickness this behaviour changes to that given by (4.11), namely the 'super-compressible regime'. Indeed, evidence for this transition is shown clearly in figure 6: at the lowest ϵ, we see in figure 6(a) that $p_{max} \sim h_{min}^{-\gamma}$; near $h_{min} = 0.002$ the solution transitions to another behaviour. At $\epsilon = 0.051$, evidence is given for $p_{max} \sim 1/\sqrt{h_{min}}$. Similarly, figure 6($b$) shows that $\ell \sim h_{min}^{1+\gamma}$, followed by a transition to $\ell \sim h_{min}^{3/2}$.

4.2. *Incompressible regime*

We now consider the incompressible regime corresponding to large ambient pressures ($\epsilon \gg 1$). In this regime, the pressure in the gas is largely constant, close to its ambient value P_0. Inhomogeneity in the gas pressure field arises from viscous forces. We therefore use the ansatz

$$p_g = 1 + \epsilon^{-1} p_{g,1}. \tag{4.12}$$

Like the super-compressible case, all three terms in the time-derivative expression in (4.2) are equally important. Substituting the pressure expansion into the scaled governing equations (2.4) and (2.9) gives us

$$h_{tt} = \mathscr{H}[p_{1,x}], \qquad h_t = (h^3 p_{1,x})_x \tag{4.13}$$

which can be further simplified using the wave-like nature of the solutions, leading to the following scalings for the pressure, P_{max}, and length scale, ℓ:

$$P_{max} \sim U^{3/2} h_{min}^{-1/2}, \qquad \ell \sim U^{1/2} h_{min}^{3/2}. \tag{4.14}$$

These scalings are identical to those derived in the super-compressible regime, despite the different physics. Figure 6 shows that at $\epsilon = 100$, the maximum pressure, p_{max} (defined here as the perturbation of the pressure from the ambient), obeys the law $p_{max} \sim 1/\sqrt{h_{min}}$, whereas $\ell \sim h_{min}^{3/2}$.

4.3. *Numerical verification and transitions*

The prefactors for the aforementioned similarity solutions can be solved for explicitly by formulating and solving similarity equations, analogous to (4.8) for the sub-compressible case. The associated similarity equations are integro-differential equations, owing to the Hilbert transform in the equation for the flow in the droplet; although such similarity equations have been solved before (Cohen *et al.* 1999), we do not carry out such analysis here. It is our view that an efficient and effective way to solve the similarity equations is to conduct a careful study of the dynamics of the

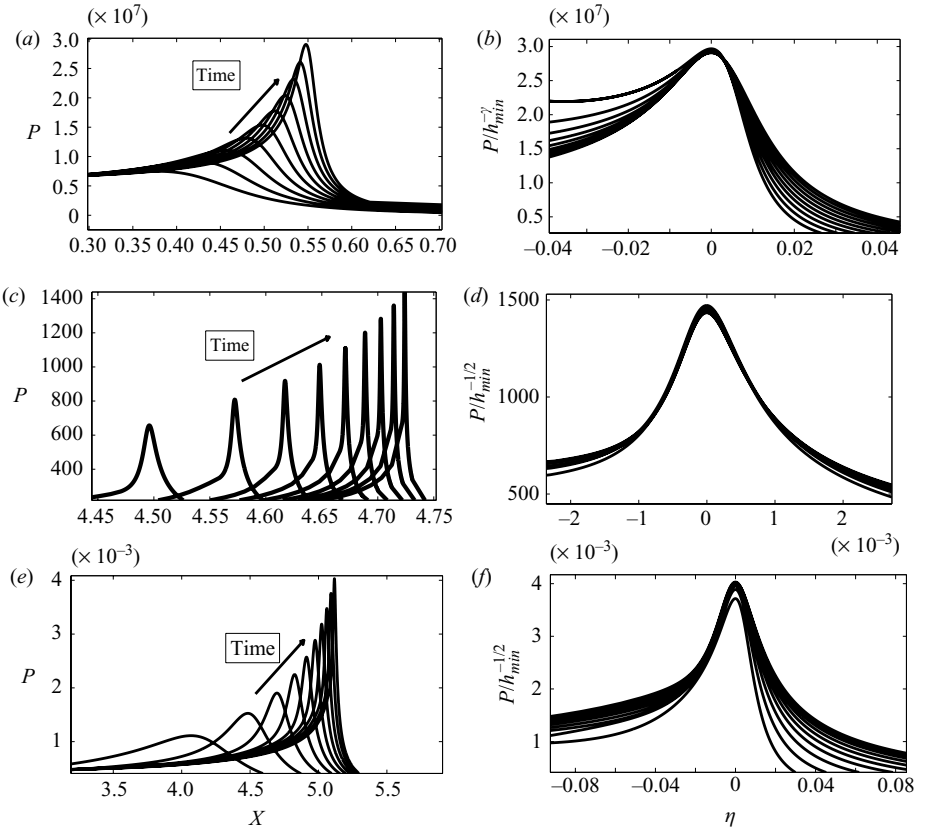

FIGURE 7. Numerical results from the (*a*, *b*) sub-compressible, (*c*, *d*) super-compressible and (*e*, *f*) incompressible regimes. (*a*, *c*, *e*) Subsequent snapshots in time of the pressure profile developing to the right of the origin. The maximum of the pressure profile can be seen to be diverging, while the characteristic length scale is tending to zero. (*b*, *d*, *f*) Scaled plot of the profiles from the left panel. The pressures are scaled by the predicted scaling and are expressed as a function of $\eta = (X - X_0(T))/(\ell(T))$ instead of X. A single universal profile $P(\eta)$ can be seen giving further evidence to the self-similar hypothesis and scalings predicted. The predictions for the various similarity laws are given in (4.9) for the top panel, (4.11) for the middle panel and (4.14) for the bottom panel.

underlying nonlinear partial differential equations, as we have done here. In view of the slow decay of the Hilbert transform kernel we ensured the accuracy of our results by changing the size of the domain integrated over, noting no significant change in the behaviour described above. Furthermore, the collapsed profiles in figure 7 are verification of the localization of the similarity equations. Nonetheless, we do not have a putative mathematical understanding of similarity equations, the matching to the outer solutions and the effect of the non-local term on the localization of the solution. This matching might be especially tricky in the compressible regime in which the outer solutions to the right and left of the kink are very different.

Figures 7 and 8 are verification of the scalings laws for the three aforementioned similarity regimes. Figure 7 demonstrates the collapse of the pressure profiles for different times on to a single universal profile, depicting the validity of the self-similarity. Similarly, figure 8 show the collapse of P_{max} and ℓ as a function of h_{min} for various ϵ, indicating that the leading-order variation in ϵ is captured by the similarity

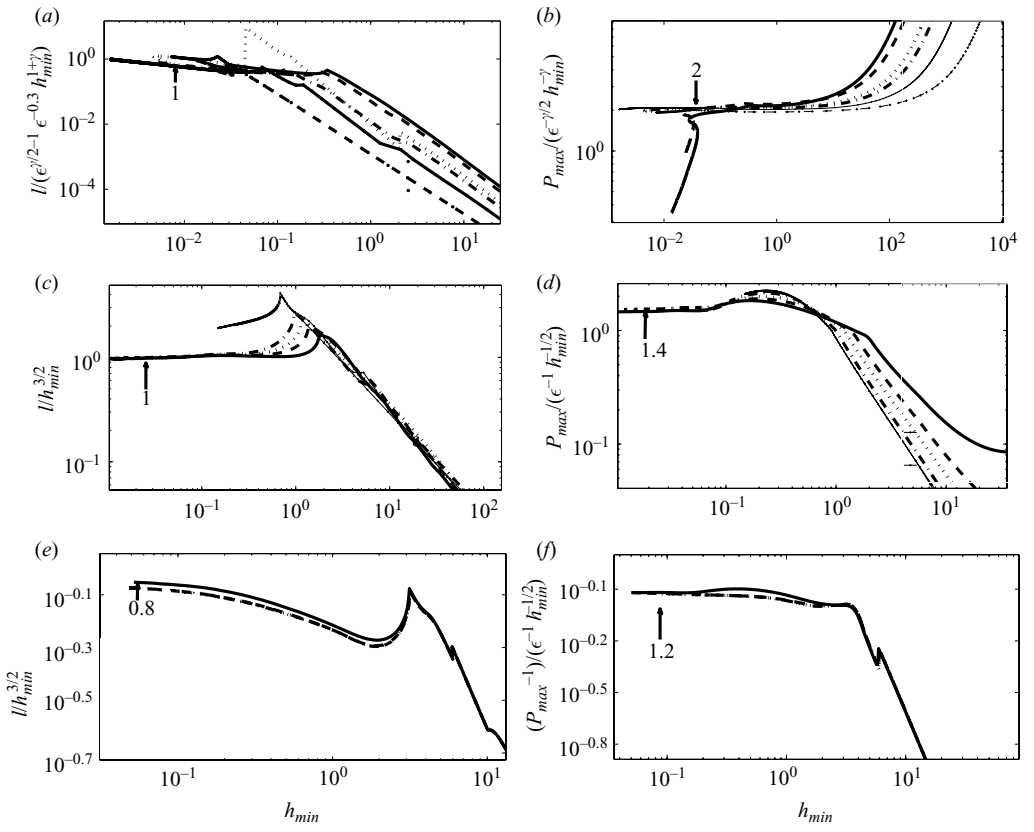

FIGURE 8. Numerical results from the (*a*, *b*) sub-compressible ($\gamma = 1.4$, $\epsilon \in [1 \times 10^{-3}, 1 \times 10^{-6}]$), (*c*, *d*) super-compressible ($\gamma = 2$, $\epsilon \in [1 \times 10^{-2}, 1 \times 10^{-9}]$) and (*e*, *f*) incompressible ($\epsilon \in [1 \times 10, 1 \times 10^{4}]$) regimes. (*a*, *c*, *e*) Log–log plot of the characteristic horizontal length scale, ℓ, divided by its predicted scaling versus the minimum height, h_{min}, for different ϵ. (*b*, *d*, *f*) Log–log plot of the maximum pressure, p_{max}, divided by its predicted scaling versus the minimum height, h_{min}, for different ϵ. For both dimensionless quantities the curves asymptote to a universal constant, indicating a verification of a universal self-similar law for both ℓ and p_{max}.

solution. Moreover, the prefactors for the scaling laws (4.9), (4.11) and (4.14) can be read off figure 8. The corresponding similarity scalings with prefactors read

$$\text{sub-compressible:} \quad P_{max} = 2.0\epsilon^{-\gamma/2} h_{min}^{-\gamma}, \qquad \ell = 1.0\epsilon^{(\gamma/2)-1} U^2 h_{min}^{1+\gamma}; \quad (4.15)$$

$$\text{super-compressible:} \quad P_{max} = 1.4\epsilon^{-1} U^{3/2} h_{min}^{-1/2}, \qquad \ell = 1.0 U^{1/2} h_{min}^{3/2}; \quad (4.16)$$

$$\text{incompressible:} \quad P_{max} = P_0 + 1.2\epsilon^{-1} U^{3/2} h_{min}^{-1/2}, \quad \ell = 0.8 U^{1/2} h_{min}^{3/2}. \quad (4.17)$$

Armed with the scaling laws and the prefactors, we are now in a position to theoretically address the transition between these similarity solutions. The transition between the sub-compressible and super-compressible regimes is predicted to occur when $A\epsilon^{-1/2} \sim f$. We have tested this in a series of simulations with $\gamma = 1.4$: there, the transition should occur when $h_{min}^{sub\text{-}super} \sim \epsilon^{0.6}$ and $P_{max}^{sub\text{-}super} \sim \epsilon^{-1.6}$. Figure 9 verifies these predicted crossovers from the sub-compressible regime over to the super-compressible regime and compares the observed scaling laws with the ones predicted by the analysis. Figure 10 shows the maximum pressure divided by its

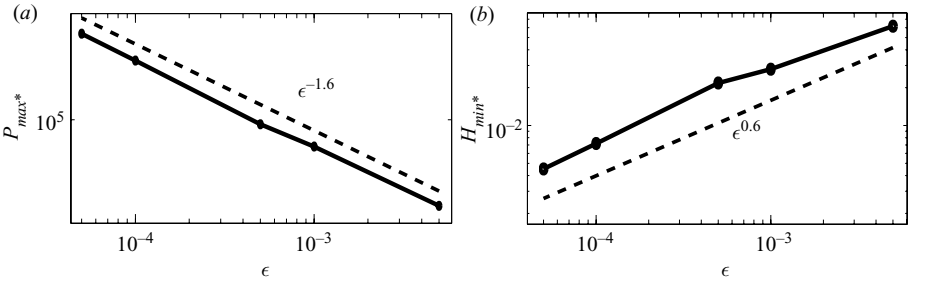

FIGURE 9. Sub-compressible to super-compressible transition: (*a*) critical pressure and (*b*) minimum height at transition as a function of ϵ. Numerical data (solid line) agree with the predicted power law (dashed line).

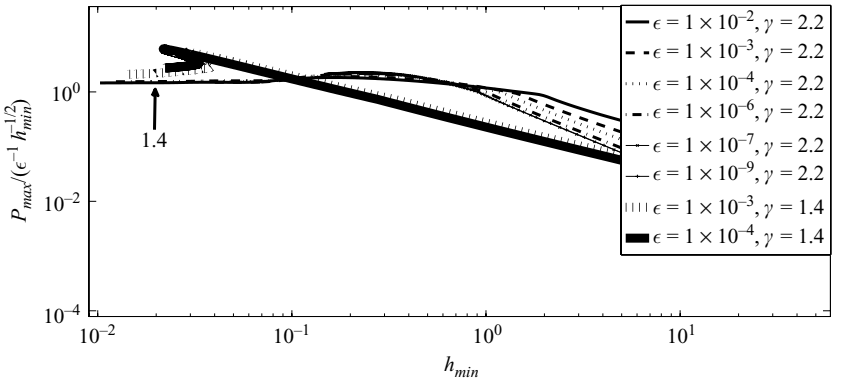

FIGURE 10. Numerical results of several super-compressible simulations and two sub-compressible solutions that transition and asymptote to the same constant as the 'pure' super-compressible solutions that start out in the super-compressible regime. The two sub-compressible solutions stand out, since the behaviour prior to transition is very different from all the other solutions in the figure.

scaling in the super-compressible regime to demonstrate the ultimate transition. The thinner curves are data from numerical simulations of solutions that enter the super-compressible regime directly. The two thick curves that stand out are results from simulations of solutions that initially start out in the sub-compressible regime, which then transition into the super-compressible regime. The plot illustrates that not only do the solutions transition to the super-compressible regime, depicted by the thick curves asymptoting to a constant, but they asymptote to the same constant as the solutions that start out in the super-compressible regime.

Once the transition to the ultimate asymptotic (super-compressible) regime occurs, the solutions lose all memory of the initial conditions from where they come. Figure 10 shows numerical simulations of a variety of different situations reaching the super-compressible regime, with $10^{-9} \leqslant \epsilon \leqslant 10^{-2}$ and different values of γ. In the figure, the thin curves represent solutions that enter the super-compressible regime directly, whereas the thick curves represent two simulations that start in the sub-compressible regime and then transition into the super-compressible regime. Strikingly, all of the solutions asymptote to the identical universal law, namely

$$P_{max} = \frac{1.4}{\epsilon \sqrt{h_{min}}}, \quad \ell = h_{min}^{3/2}, \tag{4.18}$$

where the prefactor 1.4 and unity in the expression for the pressure maximum and critical length scale, respectively, are apparent universal constants.

5. The breakdown of the similarity solutions

These similarity solutions appear to support the idea that liquid–solid contact occurs, entraining a gaseous bubble underneath. However, the self-consistency of the argument requires that we return and check whether the series of approximations that we made at the beginning of the current paper remain valid uniformly in time. A quick examination reveals that it is impossible for the solution to be uniformly consistent: independent of the regime (ϵ) every solution eventually obeys $\ell \sim h_{min}^{3/2}$; so the interfacial slopes diverge near contact. But implicit in our derivation of the equation for the gas was the lubrication theory, which requires that slopes remain small for all time. Additionally, we have neglected a number of physical effects, whose neglect may be invalid as $h_{min} \to 0$.

Here we use the universal scaling laws derived in the last section to quantitatively track the value of h_{min} the different effects can no longer be neglected and may cause a breakdown of the similarity solution. In our previous paper (Mandre *et al.* 2009) we studied the role of surface tension, which prohibits contact from occurring. Here we also include the departure from the lubrication theory, viscous effects in the liquid and nonlinear inertia in the liquid. For each effect, we present contour plots for the critical height at which this effect becomes important as a function of P_0, V, R. Underlying our analysis is a hypothesis that the parameter space can be divided into regions in which particular physical effects cause a breakdown of the similarity solution and result in a multitude of qualitatively different dynamics.

5.1. *Departure from lubrication theory*

Going back to (3.9), in the super-compressible regime the terms on the left-hand side scale as $\rho_{max} h_{min}/\ell = \rho_{max} h_{min}^{-1/2}$. On the other hand, the first term on the right-hand side originating from $\mu_g u_{g,xx}$ in (2.6) scales as $\epsilon St^{2/3} \rho_{max} h_{min}^5 p_{max}/\ell^3 = St^{2/3} \rho_{max} h_{min}^{-3/2}$. Consequently as $h_{min} \to 0$, separation of scales in the lubrication theory becomes invalid, and the $\mu_g u_{g,xx}$ term may become as large as the $\mu_g u_{g,yy}$ term. This happens when $h_{min} \sim O(St^{2/3})$ or dimensionally when $h_{min} \sim O(RSt^{4/3})$. This dimensional height, at which lubrication theory breaks down, is shown in figure 11(a) as a function of the drop radius and impact velocity. The other term on the right-hand side of (3.9) is asymptotically consistent.

5.2. *Surface tension*

The terms on the left-hand side of the drop equation (3.8) scale like $h_{min}/\ell^2 = h_{min}^{-2}$. The surface tension term $\epsilon\delta\mathscr{H}(h_{xxx})$ scales as $\epsilon\delta h_{min}^{-7/2}$ and can no longer be neglected for $h_{min} \sim O((\epsilon\delta)^{2/3})$. Dimensionally, this amounts to a minimum film thickness of $h_{min} \sim O(RSt^{8/9} We^{-2/3})$, which is plotted in figure 11(b) as a function of the drop radius and impact velocity. Note that the film thickness at which surface tension sets in or becomes important is independent of the ambient pressure P_0.

5.3. *Viscous effect*

The first term on the right-hand side of (3.8) scales as $Re^{-1} h_{min}/\ell^3 = Re^{-1} h_{min}^{-7/2}$. A breakdown ensues when $Re^{-1} h_{min}^{-3/2} \sim O(1)$ or when $h_{min} \sim O(Re^{-2/3})$. Dimensionally, $h_{min} = RSt^{2/3} Re^{-2/3}$. This dimensional height is plotted in figure 11(c). Note that the film thickness at which viscous forces becomes important is independent of the ambient pressure P_0.

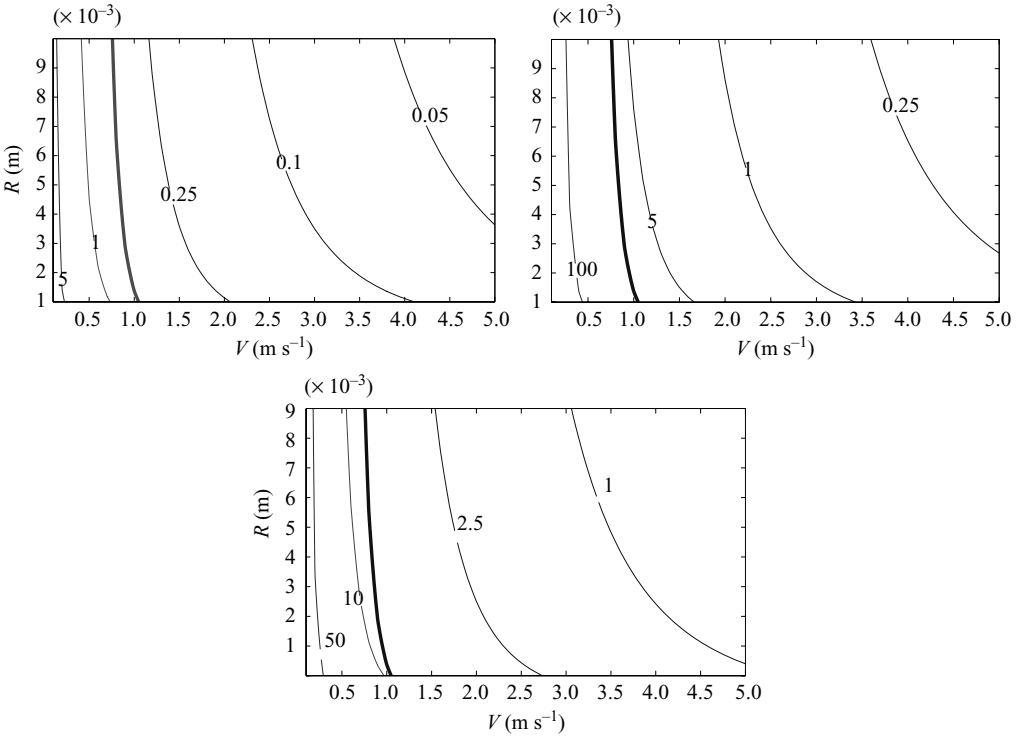

FIGURE 11. Contour plot (in nanometres) of the height at which the neglect of (*a*) corrections to lubrication theory or nonlinear-inertial effects, (*b*) surface tension or (*c*) viscous effects in the liquid becomes invalid. The thick black curve partitions parameter space into an incompressible region to its left and a compressible one to its right.

5.4. *Nonlinear inertia*

The second term on the right-hand side of (3.8) scales as $St^{1/3}h_{min}^2/\ell^3 = St^{1/3}h_{min}^{-5/2}$. Breakdown occurs when $h_{min} \sim O(St^{2/3})$ or dimensionally when $h_{min} \sim O(RSt^{4/3})$. This is identical to the scale obtained for the breakdown of lubrication theory, and the height at which this effect becomes important is shown in figure 11(*a*). Note that the film thickness at which nonlinear inertia becomes important is independent of the ambient pressure P_0.

5.5. *Non-continuum effect*

Since the film thicknesses in figure 11 are on the scale of nanometres, it is worthwhile to ask if the continuum approximation breaks down for the gas in the film. It is not obvious whether such a breakdown occurs, since the gas density is also very large when the film thickness is small. An appropriate quantitative way to analyse this is to include the leading-order non-continuum effect in the dynamics and find the criterion for that effect to become important. The leading-order non-continuum effects is that the gas slips along the boundaries according to Maxwell's slip condition (see Gopinath & Koch 2002), thus modifying the lubrication flux and adding a term $(\rho h^2 \lambda p_x)_x/2\mu$ to the right-hand side of (2.9), where λ is proportional to the mean free path of the gas. The mean free path depends on the density as $\lambda\rho = \lambda_0\rho_0$. This term is initially small; moreover, it does not change its magnitude relative to the dominant terms in (2.9) for the sub-compressible similarity solution. Once the solution

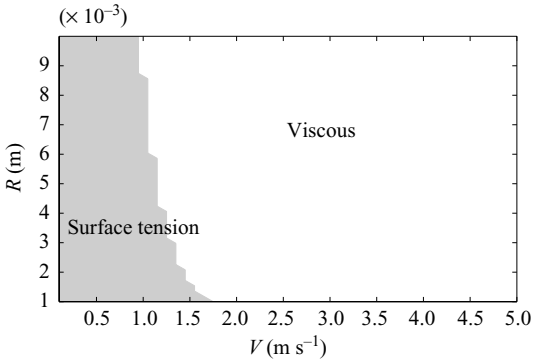

FIGURE 12. Phase diagram delineating which effect stops the similarity solution. In the shaded region, surface tension becomes important first; we have already shown (Mandre *et al.* 2009) that this causes the droplet to not impact the solid surface, skating along a thin gas layer. At high enough impact velocities, viscous forces in the liquid become important before surface tension (white region). What happens to the droplet in this region is under investigation.

transitions to the super-compressible solution, drainage is facilitated by the slip along the boundaries, and this additional drainage becomes important when dimensionally $h_{min} \sim RSt^{2/3}(\lambda_0/R)^{2\gamma/(2\gamma-1)}$. Since $\lambda_0 \sim 100$ nm, this estimate gives $h_{min} < 0.1$ nm in the best-case scenario $\gamma = 1$. Since the ultimate dynamics are independent of the ambient pressure, the conclusion holds even in reduced atmospheres. We have verified this by including the Maxwell slip term in our model and computing the solutions numerically.

6. Discussion and conclusion

The current paper has studied the dynamics of a droplet impacting a solid surface through many different stages, all occurring before surface impact occurs. The air layer causes deformation of the liquid surface, followed by the formation of a sharp kink on the surface which propagates and attempts to contact the solid surface. However, before contact, other physical effects which change the dynamics set in. We have used the universal similarity solution for the solution of the kink to derive the critical height at which three important critical effects, namely surface tension, viscous forces in the liquid and nonlinear inertia in the liquid, set in. We have demonstrated that each of these effects sets in at a critical height which depends on the droplet radius R and impact velocity V but not the ambient pressure P_0. As to date, the authors are unaware of any visualization of the droplet interface as it approaches a substrate (solid or liquid), such an experiment would provide an ideal test for the various hypotheses made here.

Figure 12 summarizes our results in a phase diagram of droplet velocity and radius. We have coloured the phase diagram according to the physical effect that sets in at the largest gap thickness. At low impact velocities, surface tension becomes important first (shaded grey), whereas at higher velocities viscous forces in the liquid dominate (shaded white). Our previous paper has demonstrated that when surface tension becomes important, contact with the liquid surface is completely prohibited, and instead the droplet skates along a thin air layer of thickness $2.54RSt^{8/9}We^{-2/3}$. Here we see that this result is self-consistent at velocities below $\sim 1\,\mathrm{m\,s^{-1}}$, with the precise value depending on droplet radius. Above the threshold depicted in figure 12, viscous forces in the liquid become important first and will modify the self-similar

dynamics before surface tension forces. The resulting dynamics of the liquid interface in this regime is not yet known. It is noteworthy that the only role we have uncovered for the gas pressure P_0 is its effect on the dimple height; neither the surface tension transition nor the viscous transition depends on P_0, and hence neither are sufficient to explain the pressure dependence observed in Xu *et al.* (2005). There are a number of other physical effects that might also become important, including (i) heat transfer in the gas, which affects the gas equation of state, and (ii) mass diffusion from the gas into the liquid. Whether any of these effects conspires with surface tension and viscous forces in the liquid to give a mechanism of sheet formation remains to be seen.

This research was supported by the National Science Foundation through the Division of Mathematical Sciences and the Harvard MRSEC.

Appendix. Numerical method

The numerical method of choice to solve these equations is dictated by the stiffness of (3.11) and (3.12). In the spirit of finite-difference methods, we define a discrete spatial grid defined by $x_j = x_0 + j\Delta x$, where x_0 is the x-coordinate of the first grid point and Δx is a constant grid spacing. The solution is approximated only at these grid points and at times $t_0, t_1, t_2, \ldots, t_n$, and we use the notation $\phi_j^n = \phi(x_j, t_n)$ for arbitrary functions ϕ. For stability, an explicit finite-difference method for the drop equation (3.11) requires a time step $\Delta t \propto \Delta x^{3/2}$ for a given Δx. Similarly, for the compressible lubrication equation (3.12) the condition is $\Delta t \propto \Delta x^2$. Anticipating a small spatial scale to develop as the solution evolves, a fine grid is required to resolve it. This imposes a very strict constraint on the allowable time step and makes the computation prohibitively slow. Instead of explicit methods, we opt for semi-implicit schemes to manage numerical instabilities, allowing us to take arbitrary time steps. In particular, we substitute the equation of state (3.10) in the compressible lubrication equation (3.12) and at each time step solve for the change in the gas density $\Delta\rho_j = \rho_j^{n+1} - \rho_j^n$, given the change $\Delta h_j = h_j^{n+1} - h_j^n$ in the film thickness. The lubrication equations is linearized for small $\Delta\rho_j$ to obtain a sparse linear system of equations,

$$\begin{aligned}
&\Delta\rho_j \left[h_j^{n+1} + (\gamma+1)\rho_j^{n\gamma}(R_{j+1/2} + R_{j-1/2})\right] - \Delta\rho_{j-1}(\gamma+1)\rho_{j-1}^{n\gamma} R_{j-1/2} \\
&\quad - \Delta\rho_{j+1}(\gamma+1)\rho_{j+1}^{n\gamma} R_{j+1/2} = \rho_j^n \Delta h_j + 2R_{j+1/2}\left[\rho_{j+1}^{n(\gamma+1)} - \rho_j^{n(\gamma+1)}\right] \\
&\quad - 2R_{j-1/2}\left[\rho_j^{n(\gamma+1)} - \rho_{j-1}^{n(\gamma+1)}\right], \qquad \text{(A 1)}
\end{aligned}$$

where

$$R_{j+1/2} = \frac{\epsilon\gamma\Delta t}{12(\gamma+1)\Delta x^2}\left(\frac{1}{h_{j+1}^{n3}} + \frac{1}{h_j^{n3}}\right)^{-1}. \qquad \text{(A 2)}$$

At the boundary points $\Delta\rho_j$ is set to zero. These equations can be solved for $\Delta\rho_j$ in $O(N)$ computation per time step.

Once $\Delta\rho_j$ is found, it is used to compute p_j^{n+1} to be substituted in the Hilbert transform in (3.11) to advance h to the next time step. Although the Hilbert transform is linear, applying a semi-implicit method based on finite differences is not optimal because the linear system generated to solve for Δh_j is not sparse and would require

at least $O(N^2)$ computation. Instead, transforming to Fourier space as

$$h_j^n = \frac{x^2}{2} + \sum_{k=-N/2}^{N/2-1} \hat{h}_k^n \exp\left(\frac{2\pi i k x_j}{L}\right), \quad h_{t,j}^n = \sum_{k=-N/2}^{N/2-1} \hat{v}_k^n \exp\left(\frac{2\pi i k x_j}{L}\right), \tag{A 3}$$

where L is the length of the domain, allows for the stiffness resulting from the surface tension term to be integrated analytically. The Fourier coefficients satisfy

$$\left.\begin{aligned} \hat{h}_k^{n+1} &= \hat{h}_k^n \cos\omega_k \Delta t + \frac{\hat{v}_k^n}{\omega_k} \sin\omega_k \Delta t + \hat{p}_k^n \frac{\Delta t^2}{2}, \quad k \neq 0, \\ \hat{v}_k^{n+1} &= -\hat{h}_k^n \omega_k \sin\omega_k \Delta t + \hat{v}_k^n \cos\omega_k \Delta t + \hat{p}_k^n \Delta t, \quad k \neq 0, \\ \hat{h}_0^{n+1} &= \hat{h}_0^n + \hat{v}_0^n \Delta t + \hat{p}_0^n \frac{\Delta t^2}{2}, \quad \hat{v}_0^{n+1} = \hat{v}_0^n + \hat{p}_0^n \Delta t, \end{aligned}\right\} \tag{A 4}$$

where $\hat{p}_k^n$ denote the discrete Fourier transform of p_j^n as

$$p_j^n = \sum_{k=-N/2}^{N/2-1} \hat{p}_{g,k}^n \exp\left(\frac{2\pi i k x_j}{L}\right) \tag{A 5}$$

denotes the Fourier transform of the gas pressure and $\omega_k = \sqrt{8\pi^3 \sigma k^3/\rho_l L^3}$. The forward and inverse Fourier transforms can be carried out in $O(N \log N)$ computation using fast Fourier transform algorithms. Owing to the Fourier expansion, the interface perturbations from a parabolic shape are strictly speaking periodic. However, we chose a large enough simulation domain to ensure that the perturbation decayed towards the boundary, and this periodicity does not affect the solution, as verified by doubling the domain length.

We implemented an adaptive time-stepping strategy to traverse any fast transients without losing accuracy. The error in each time step was estimated from a Richardson extrapolation, i.e. by comparing the solution obtained by a time step Δt with that obtained by taking two time steps of duration $\Delta t/2$ each. If the maximum value of the relative error was larger than a preset tolerance (usually set to 10^{-3}), the time step was reduced by a factor of 2.

The spatial grid was also adapted depending on the current spatial scale of the solution. The spatial scale was estimated as the distance between two landmarks of the solution; examples of the landmarks we used are the minimum of h, the maximum of p and the extrema of h_t. The choice of landmarks depended on the particular solution under consideration. The number of points in the grid were doubled if the distance between the chosen landmarks spanned less than a preset number (usually 40) of grid points. The refined solution is found by interpolating the unrefined solution using cubic splines.

Each simulation is started with the initial condition

$$h_j^0 = H_0 + \frac{x_j^2}{2}, \quad h_{tj} = -1, \quad \rho_j = 0, \tag{A 6}$$

for sufficiently large H_0. The particular H_0 we used depended on the parameters, and the solution was accepted only if doubling the value of H_0 yielded the same solution to three significant digits.

REFERENCES

Bach, G. A., Koch, D. L. & Gopinath, A. 2004 Coalescence and bouncing of small aerosol droplets. *J. Fluid Mech.* **518**, 157–185.

Bowden, F. P. & Field, J. E. 1964 The deformation of solids by liquid impact, by solid impact and by shock. *Proc. R. Soc. Lond.* A **282**, 331–352.

Bussmann, M., Chandra, S. & Mostaghimi, J. 2000 Modeling the splash of a droplet impacting a solid surface. *Phys. Fluids* **12**, 3121.

Cohen, I., Brenner, M. P., Eggers, J. & Nagel, S. R. 1999 Two fluid drop snap-off problem: experiments and theory. *Phys. Rev. Lett.* **83**, 1147.

Deegan, R. D., Brunet, P. & Eggers, J. 2008 Complexities of splashing. *Nonlinearity* **21**, C1–C11.

Field, J. E., Dear, J. P. & Ogren, J. E. 1989 The effects of target compliance on liquid drop impact. *J. Appl. Phys.* **65**, 533–540.

Gopinath, A. & Koch, D. L. 2002 Collision and rebound of small droplets in an incompressible continuum gas. *J. Fluid Mech.* **454**, 145–201.

Haller, K. K., Poulikakos, D., Ventikos, Y. & Monkewitz, P. 2003 Shock wave formation in droplet impact on a rigid surface. *J. Fluid. Mech.* **490**, 1–14.

Jenkins, D. C. & Booker, J. D. 1960 In *Aerodynamic Capture Particles* (ed. E. G. Richardson), pp. 97–103. Permagon.

Lesser, M. B. 1981 Analytic solutions of liquid-drop impact problems. *Proc. R. Soc. Lond.* A **377**, 289–308.

Lesser, M. B. & Field, J. E. 1983 The impact of compressible liquids. *Annu. Rev. Fluid Mech.* **15**, 97–122.

Levin, Z. & Hobbs, P. V. 1971 Splashing of water drops on solid and wetted surfaces. *Philos. Trans. R. Soc. Lond.* A **269**, 555.

Mandre, S., Mani, M. & Brenner, M. P. 2009 Precursors to splashing of liquid droplets on a solid surface. *Phys. Rev. Lett.* **102**, 134502-1–134502-4.

Pan, K. L. & Law, C. K. 2007 Dynamics of droplet-film collision. *J. Fluid Mech.* **587**, 1–22.

Rein, M. 1993 Phenomena of liquid drop impact on solid and liquid surfaces. *Fluid Dyn. Res.* **12**, 6193.

Rein, M. & Delplanque, J. P. 2008 The role of air entrainment on the outcome of drop impact on a solid surface. *Acta Mech.* **201**, 105–118.

Smith, F. T., Li, L. & Wu, G. X. 2003 Air cushioning with a lubrication inviscid balance. *J. Fluid Mech.*, 291–318.

Stow, C. D. & Hadfield, M. G. 1981 An experimental investigation of fluid flow resulting from the impact of a water drop with an unyielding dry surface. *Proc. R. Soc. Lond.* A **373**, 419.

Taylor, G. I. & Saffman, P. G. 1957 Effects of compressibility at low Reynolds number. *J. Aeronaut. Sci.* **24**, 553.

Thoroddsen, S. T., Etoh, T. G. & Takehara, K. 2003 Air entrapment under an impacting drop. *J. Fluid Mech* **478**, 125–134.

Thoroddsen, S. T., Etoh, T. G., Takehara, K., Ootsuka, N. & Hatsuki, Y. 2005 The air bubble entrapped under a drop impacting on a solid surface. *J. Fluid Mech.* **545**, 203–212.

Xu, L., Zhang, W. W. & Nagel, S. R. 2005 Drop splashing on a dry smooth surface. *Phys. Rev. Lett.* **94**, 184505.

Yarin, A. L. & Weiss, D. A. 1995 Impact of drops on solid surfaces: self similar capillary waves and splashing as a new type of kinetic discontinuity. *J. Fluid Mech.* **283**, 141.